

“This document is the Accepted Manuscript version of a Published Work that appeared in final form in *Nano Letters*, copyright © American Chemical Society after peer review and technical editing by the publisher. To access the final edited and published work see:

<https://dx.doi.org/10.1021/acs.nanolett.5b05125>”

# Twin-induced InSb nanosails: a convenient high mobility quantum system

*María de la Mata,<sup>1,‡</sup> Renaud Leturcq,<sup>2,3,‡\*</sup> Sébastien R. Plissard,<sup>4</sup> Chloé Rolland,<sup>2,‡</sup> César Magén,<sup>5</sup> Jordi Arbiol,<sup>1,6,\*</sup> and Philippe Caroff,<sup>2,7,\*</sup>*

<sup>1</sup>Catalan Institute of Nanoscience and Nanotechnology (ICN2), CSIC and The Barcelona Institute of Science and Technology, Campus UAB, Bellaterra, 08193 Barcelona, Spain

<sup>2</sup>Institut d'Électronique, de Microélectronique et de Nanotechnologie, UMR CNRS 8520, Avenue Poincaré, C.S. 60069, 59652 Villeneuve d'Ascq, France

<sup>3</sup>Materials Research and Technology (MRT) Department, Luxembourg Institute of Science and Technology (LIST), 5, avenue des Hauts-Fourneaux, L-4362 Esch-sur-Alzette, Luxembourg

<sup>4</sup>CNRS-Laboratoire d'Analyse et d'Architecture des Systèmes (LAAS), Université de Toulouse, 7 avenue du colonel Roche, 31400 Toulouse, France

<sup>5</sup>Laboratorio de Microscopías Avanzadas (LMA), Instituto de Nanociencia de Aragon (INA) - ARAID, and Departamento de Física de la Materia Condensada, Universidad de Zaragoza, 50018 Zaragoza, Spain

<sup>6</sup>Institució Catalana de Recerca i Estudis Avançats (ICREA), 08010 Barcelona, Catalonia, Spain

1  
2  
3 <sup>7</sup>Department of Electronic Materials Engineering, Research School of Physics and Engineering,  
4  
5  
6 The Australian National University, Canberra, ACT 0200, Australia  
7  
8  
9  
10  
11  
12  
13

14  
15 ABSTRACT  
16  
17

18  
19 Ultra-narrow bandgap III-V semiconductor nanomaterials provide a unique platform for realizing  
20  
21 advanced nanoelectronics, thermoelectrics, infra-red photodetection and quantum transport  
22  
23 physics. In this work we employ molecular beam epitaxy to synthesize novel nanosheet-like InSb  
24  
25 nanostructures exhibiting superior electronic performance. Through careful morphological and  
26  
27 crystallographic characterization we show how this unique geometry is the result of a single  
28  
29 twinning event in an otherwise pure zinc blende structure. Four-terminal electrical measurements  
30  
31 performed in both the Hall and van der Pauw configurations reveal a room temperature electron  
32  
33 mobility greater than  $12,000 \text{ cm}^2 \cdot \text{V}^{-1} \cdot \text{s}^{-1}$ . Quantized conductance in a quantum point contact  
34  
35 processed with a split-gate configuration is also demonstrated. We thus introduce InSb  
36  
37 ‘nanosails’ as a versatile and convenient platform for realizing new device and physics  
38  
39 experiments with a strong interplay between electronic and spin degrees of freedom.  
40  
41  
42  
43  
44  
45

46  
47 KEYWORDS III-V Semiconductor, Nanowires, Molecular Beam Epitaxy, Hall measurements,  
48  
49 Quantum Point Contact, Cs-corrected Scanning Transmission Electron Microscopy.  
50  
51

52  
53  
54 High-quality narrow bandgap III-V semiconductor nanostructures hold promise for applications  
55  
56 in infra-red optoelectronics<sup>1,2</sup>, low-power nanoelectronics<sup>3,4</sup> and quantum physics<sup>5</sup>. Until now,  
57  
58  
59  
60

1  
2  
3 reports have focused on the nanowire geometry which has been used to demonstrate direct  
4 integration on silicon<sup>6</sup>, gate-all-around (tunnel) field effect transistors<sup>7-9</sup>, efficient IR  
5 photodetection,<sup>10, 11</sup> lasing<sup>12-14</sup> and enhanced thermoelectric performance<sup>15-20</sup>.  
6  
7  
8  
9

10  
11 With the narrowest bandgap among the III-V semiconductors, InSb is characterized by an  
12 extremely low effective carrier mass and therefore has the potential to realize some of the highest  
13 values of electron mobility among all semiconductors. Coupled with the largest Landé g-factor  
14 of all semiconductors,<sup>21</sup> and the fact that peak electron velocity occurs at relatively low electric  
15 fields, InSb is an ideal material for high speed and low power nanoelectronics<sup>22</sup> and 0D/1D  
16 electron or hole systems for quantum transport physics<sup>23-25</sup>. High quality InSb nanowires have  
17 already been shown to enable fast manipulation of spin-orbit qubits<sup>24, 26</sup> and have played a key  
18 role in the search for the elusive Majorana fermion<sup>27-29</sup>.  
19  
20  
21  
22  
23  
24  
25  
26  
27  
28  
29  
30

31 The epitaxial growth conditions and crystal quality of antimonide nanostructures differ  
32 significantly from those of all other III-Vs due to both the low vapor pressure of Sb and its action  
33 as a surfactant<sup>30</sup>. On one hand, these specificities make growth of InSb free-standing  
34 nanostructures challenging due to the necessity of providing nanowire ‘stems’ to nucleate them  
35 away from the substrate<sup>31</sup>, impractically slow growth rates in the axial direction<sup>32</sup>, and the  
36 existence of very narrow ‘sweet spot’ in the growth parameter space<sup>33</sup>. On the other hand, these  
37 special growth conditions guarantee a perfect crystal structure independently of the growth  
38 technique<sup>34-37</sup> a total absence of tapering for nanowires thanks to a very low nucleation  
39 probability on their {110} sidewalls and the opportunity to tailor the morphology, to deliver  
40 geometries such as diamond-shaped free-standing 3D nanostructures<sup>33, 38</sup>, or nanocrosses<sup>39, 40</sup>.  
41  
42  
43  
44  
45  
46  
47  
48  
49  
50  
51  
52  
53  
54  
55 While antimonide nanocrystals usually lack planar defects perpendicular to the growth direction,  
56 the appearance of crystallographic defects in other directions can induce changes in the geometry  
57  
58  
59  
60

1  
2  
3 of the overall system rather than promoting a crystal phase transition, explaining the formation of  
4 tilted nanowires<sup>41</sup>, branched nanostructures<sup>42</sup> or kinking phenomena<sup>43</sup>. Despite these  
5  
6 achievements, the nanowire geometry has proven impractical for the realization of multi-terminal  
7  
8 devices such as Hall bars<sup>44,45</sup>, quantum point contacts or Aharonov-Bohm rings<sup>46</sup>. Realizing  
9  
10 nanosheets of this material while keeping the advantages already demonstrated by nanowires  
11  
12 would thus open the way to more advanced device geometries<sup>47</sup>, still enable advanced  
13  
14 heterostructures<sup>48</sup>, while also significantly easing the device fabrication process<sup>49</sup>. There are  
15  
16 currently however few reports of free-standing III-V nano-sheets and the majority of these  
17  
18 examples contain at least a few stacking defects perpendicular to their vertical growth axis<sup>50-54</sup>.  
19  
20  
21  
22  
23  
24

25  
26 Here we show that InSb nanosheets in the form of a vertical nanosail can be grown epitaxially  
27  
28 from an InAs ‘mast’ acting as a stem, with a thickness controlled by the seed particle, two large  
29  
30 atomically flat {110} surfaces and a highly faceted geometry. Growth is possible using the two  
31  
32 main epitaxy techniques, i.e. metalorganic vapour phase epitaxy (MOVPE) and molecular beam  
33  
34 epitaxy (MBE), but only the latter is detailed here. The nanosail crystal structure grown by MBE  
35  
36 is confirmed to be pure zinc blende with only a single isolated twin boundary event on the lateral  
37  
38 side. It is found that the single twin drives the crystal to change its geometry and expand to  
39  
40 create the observed 2D-like morphology. We then proceed with studying its key electronic  
41  
42 figures of merit such as mobility and carrier concentration using a multi-terminal device  
43  
44 configuration. A very high mobility above  $12\,000\text{ cm}^2\cdot\text{V}^{-1}\text{s}^{-1}$  is unambiguously determined both  
45  
46 at low temperature and room temperature. Finally, we demonstrate for the first time quantized  
47  
48 conductance in a bottom-up InSb nanomembrane in a quantum point contact (QPC)<sup>55,56</sup>, in the  
49  
50 absence of an in-plane applied magnetic field<sup>57</sup>.  
51  
52  
53  
54  
55  
56  
57  
58  
59  
60

1  
2  
3 The InAs/InSb nanowire/nanosail heterostructures were grown on InP (111)B *via* a gold-  
4 assisted vapor-liquid-solid mechanism in a Riber 32-P gas-source molecular beam epitaxy  
5 (MBE) system following a methodology very similar to that reported by Thelander *et al.*<sup>37</sup>. The  
6 structure consists, from bottom to top, of a short InP/InAs stem followed by the InSb segment.  
7  
8 The general morphology and faceting was evaluated using a Zeiss Ultra 55 SEM while  
9 mechanically detached nanostructures were studied by atomic resolution high angle angular  
10 dark-field scanning transmission electron microscopy (HAADF-STEM) using a probe corrected  
11 FEI Titan 60–300 equipped with a high brightness field emission gun (XFEG) and a CETCOR  
12 corrector from CEOS. All the 3D atomic models here presented have been created using the  
13 Rhodius software<sup>58,59</sup>. Back-gated devices were fabricated by transferring the nanosails onto a  
14 thermally oxidized highly-doped Si substrate. Low resistive ohmic contacts were then defined by  
15 electron beam lithography on ammonium sulphide passivated nanostructures. For the quantum  
16 point contact (QPC) device, two ohmic contacts are realized, followed by the deposition of a 10  
17 nm HfO<sub>2</sub> conformal gate dielectric layer by atomic layer deposition, and two split gates defined  
18 by electronic lithography. Variable temperature magneto-transport experiments were performed  
19 in a helium cryostat with a variable temperature insert allowing measurements from 2.1 to 300  
20 K, and magnetic field up to 7 T. The Hall and van der Pauw measurements were performed using  
21 the lock-in technique. The quantum point contact measurements were performed with a constant  
22 d.c. bias voltage. Full growth, characterization and processing details are given in Supporting  
23 Information SA.

24  
25  
26  
27  
28  
29  
30  
31  
32  
33  
34  
35  
36  
37  
38  
39  
40  
41  
42  
43  
44  
45  
46  
47  
48  
49  
50  
51  
52 Figure 1(a) presents an as-grown InAs/InSb nanowire ensemble containing nanosails  
53 structures. Growth here consisted of axial InP/InAs heterostructure stems topped with an InSb  
54 segment. Only the bottom InAs stem and InSb sections are visible in this scanning electron  
55  
56  
57  
58  
59  
60

1  
2  
3 microscopy (SEM) image. It is clear that while some InAs/InSb heterostructures remain in the  
4  
5 shape of standard nanowires<sup>35</sup> or even diamond-shaped crystallites<sup>33,38</sup>, a significant proportion  
6  
7 of the InSb segments form flat sail-like nanosheets, which we henceforth refer to as ‘nanosails’.  
8  
9 The variation observed here may be related to the stochastic nature of the Au dewetting process  
10  
11 which produces a distribution of seed diameters and areal densities and the extreme sensitivity of  
12  
13 free-standing InSb nanostructures to local growth conditions<sup>31-33</sup>. An illustration of this intrinsic  
14  
15 sensitivity of InSb to local growth conditions is illustrated in Supporting Figure S1. It can  
16  
17 therefore be inferred that the specific nucleation event leading to this original InSb nanosail  
18  
19 morphology has a small probability of occurrence under the studied growth conditions. The  
20  
21 percentage of nanosails to nanowires is measured to be 5.6% (see Supporting Figure S3). The  
22  
23 ease of obtaining the nanosail geometry is further confirmed in Supporting Figure S2 where the  
24  
25 same nanostructures are grown by MOVPE (see Supporting Figure S2).  
26  
27  
28  
29  
30  
31  
32  
33  
34  
35  
36  
37  
38  
39  
40  
41  
42  
43  
44  
45  
46  
47  
48  
49  
50  
51  
52  
53  
54  
55  
56  
57  
58  
59  
60

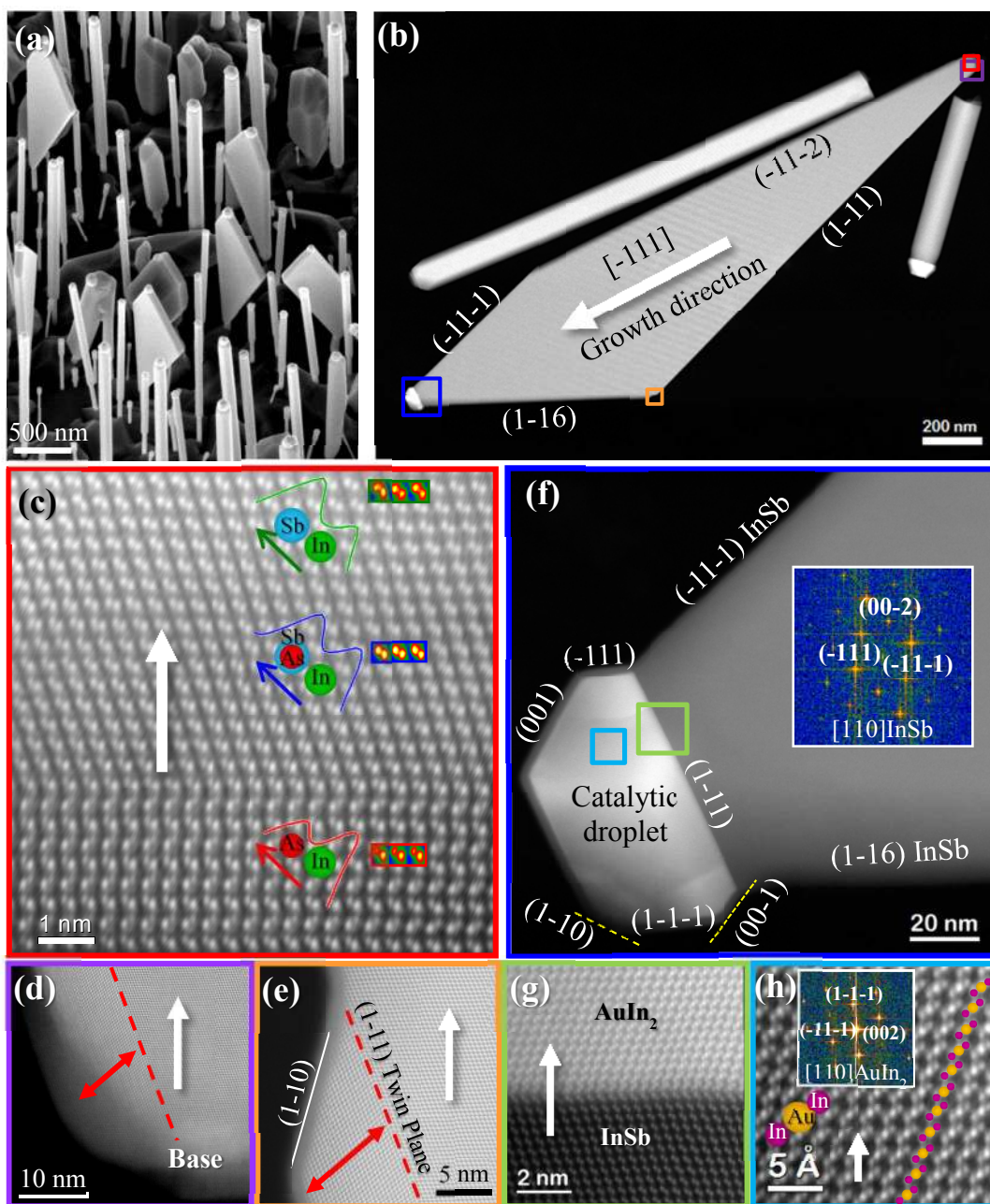


**Figure 1.** General morphology and crystal structure. (a) SEM image (30° tilt) showing a representative overview of an as-grown InAs/InSb ensemble containing nanosails. (b) Low magnification HAADF image of a nanosail with the regions magnified in c-h indicated by colored squares (c) Atomic resolution HAADF image of the base of the nanosail (growth direction is vertical) showing both WZ InAs and ZB InSb. Red, blue and green curves



1  
2  
3 correspond to intensity profiles taken along individual dumbbells in order to determine polarity,  
4 which was found to be B-polar for both InAs and InSb. (d,e) High resolution images of the twin  
5 boundary extending parallel to the  $\{111\}$  lateral facet, from the base (d) to its termination (e),  
6 where the twinned segment is of constant width (highlighted by the red arrow). (f) Z-contrast  
7 image of the nanosail's tip, showing the facets of the AuIn<sub>2</sub> seed particle. A fast Fourier  
8 transform (FFT) of the InSb nanosail structure is inset (g) Atomically resolved image of the  
9 interphase between the InAs nanosail structure (darker) and the AuIn<sub>2</sub> single crystalline seed  
10 particle (brighter) (h) Atomic resolution image of the AuIn<sub>2</sub> structure with FFT inset. Note that  
11 the white arrow points indicate the  $[\bar{1}11]$  growth direction.  
12  
13  
14  
15  
16  
17  
18  
19  
20  
21  
22  
23  
24

25  
26 After mechanical dispersion on a holey carbon grid, the nanosails facets were indexed using  
27 atomically resolved High Angle Annular Dark Field (HAADF) Scanning Transmission Electron  
28 Microscopy (STEM). The primary facets were determined to be  $\{110\}$  type bordered by facets of  
29 mostly of  $\{111\}$  type (Figure 1(b)). Considering the base of the nanosail, Figure 1(c), we observe  
30 that the narrow InAs 'mast' segment below the InSb section crystallizes in the wurtzite (WZ)  
31 structure while the rest of the sail (composed of pure InSb) presents a pure zinc-blende (ZB)  
32 structure (Figure 1(c)). The polarity of the growth direction is further confirmed to be anionic or  
33 'B' type by measuring the intensity profile along dumbbells (colored curves in Figure 1(c))<sup>60</sup>.  
34 This analysis also reveals the presence of As in the first nanometers of the InSb ZB base. Indeed  
35 the relative intensity inversion observed (i.e., InAs shows As polarity, being In the heavier  
36 constituent, red plot in Figure 1(c); while InSb presents Sb polarity being Sb the heavier, green  
37 plot in Figure 1(c)) demonstrates that the interface between materials is not abrupt, as reported  
38 previously for InAs/InSb nanowires<sup>61</sup>. Further strain analysis shown in Supporting Figure S4  
39 along with EELS measurements confirm the alloying at the InAs/InSb interface over a few  
40  
41  
42  
43  
44  
45  
46  
47  
48  
49  
50  
51  
52  
53  
54  
55  
56  
57  
58  
59  
60

1  
2  
3 nanometers. Focusing now on the InSb nanosail itself, all investigated samples were  
4  
5 characterized by a pristine ZB structure with the exception of a single longitudinal twin boundary  
6  
7 located at the base (see Figure 1(e)) and extending parallel to one of the {111} lateral facets of  
8  
9 the structures, disappearing at the corner (Figure 1(f)) where the new facet shrinking the  
10  
11 structure starts to develop. This single structural defect will be discussed in details in the  
12  
13 following and in Supporting Information..  
14  
15  
16

17  
18 Post-growth, the seed particles were found to be single AuIn<sub>2</sub> crystals with a cubic Fm3-m  
19  
20 structure (Figure 1 (g,h)), and perfectly lattice-matched to the nanosail: (-11-1) [110] AuIn<sub>2</sub> || (-  
21  
22 111)[110] InSb. The AuIn<sub>2</sub> composition is in agreement with the pseudo binary eutectic region  
23  
24 of the Au-In-Sb ternary phase diagram, as discussed in previous works<sup>35, 36, 62</sup>. The interface  
25  
26 between the sail and the alloy metal particle is atomically flat, and there is no evidence of gold  
27  
28 diffusion within the nanosail structure. The particle exhibits low-index facets, as shown Figure  
29  
30 1(d), similar to those previously reported for InSb NWs<sup>61</sup>.  
31  
32  
33  
34  
35  
36  
37  
38  
39  
40  
41  
42  
43  
44  
45  
46  
47  
48  
49  
50  
51  
52  
53  
54  
55  
56  
57  
58  
59  
60

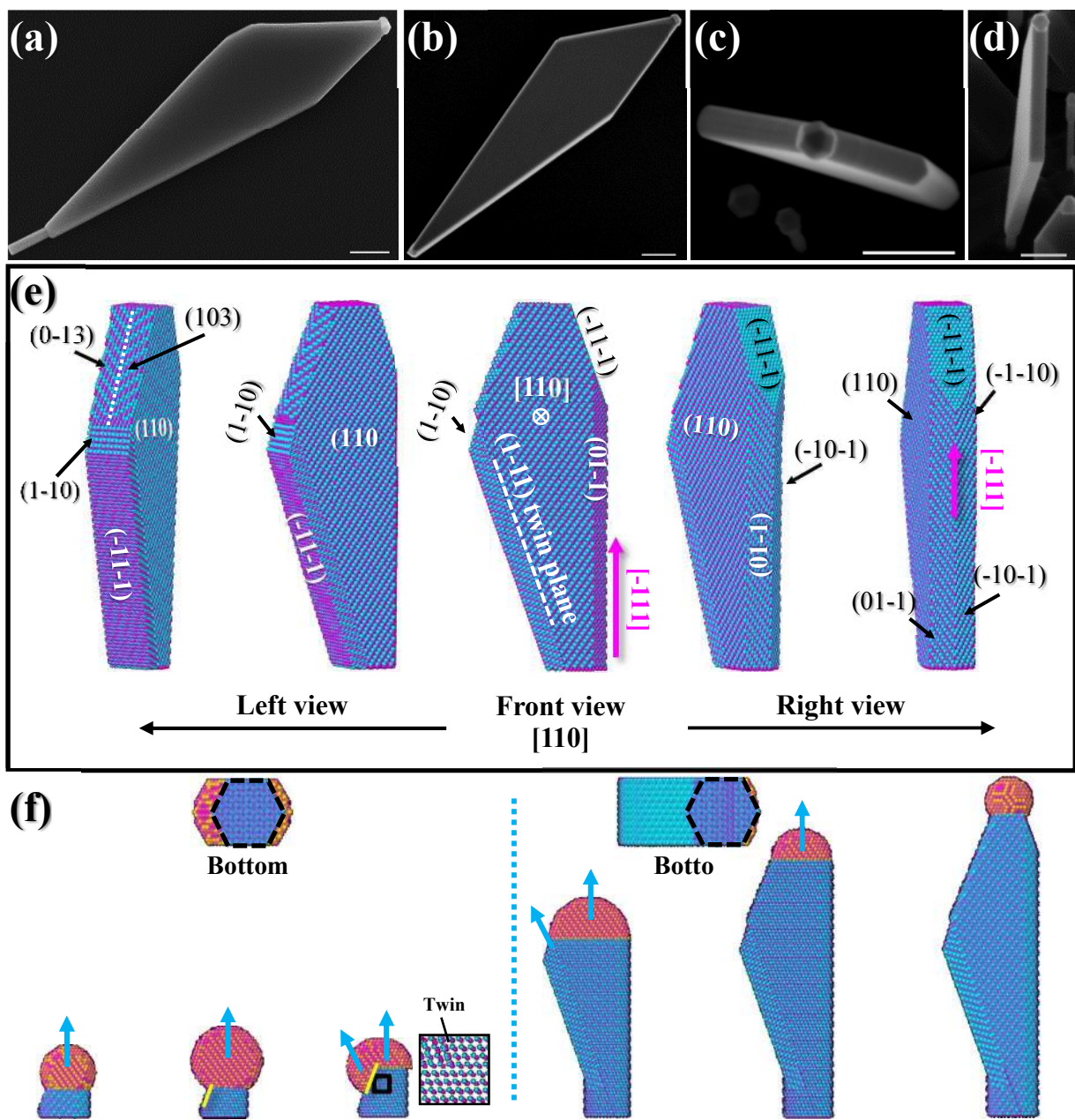


**Figure 2. 3D facet structure and growth scenario.** (a-d) Various SEM images of nanosails either lying flat on a silicon host substrate (a,b) or free-standing (c,d), revealing the general geometry and small variations in shape. Scale bars are 200 nm for (a-d). (e) Atomic 3D model of the nanosail illustrating its main facets and geometry. (f) Evolution of the nanosail geometry.

1  
2  
3 Having established that our nanostructures were of the highest crystalline quality we then  
4  
5 further investigate their faceting and 3D geometry using both experimental data and 3D atomistic  
6  
7 modelling. From the analysis of a combination of SEM images taken with both titled view and  
8  
9 plane view together with STEM images in different zone axes, a precise 3D atomistic model was  
10  
11 built. The final nanosail geometry was found to vary slightly depending on its development stage  
12  
13 (Figure 2 (a)-(d) and Supporting Figure S7) but all nanosails were characterized by several  
14  
15 common features, discussed below. Similarities among nanowires and nanosails cannot be  
16  
17 neglected and, indeed, as well as growing along the same direction, i.e.,  $[-111]$ , both  
18  
19 architectures shown a partial common faceting based on  $\{110\}$  planes. For the nanosails, the  
20  
21 frontal and back facets always correspond to  $\{110\}$  planes, i.e.,  $(110)$  and  $(-1-10)$ , as illustrated  
22  
23 in the  $[110]$  front view in Figure 2(e), but also the vertical side of the nanosail is composed by  
24  
25 two different  $\{110\}$  planes (i.e.,  $(01-1)$  and  $(-10-1)$ ). The bottom lateral side expanding outwards  
26  
27 and running parallel to the observed twin boundary, belongs to the  $(-11-1)$  plane, as well as the  
28  
29 upper parallel facet. It is noteworthy that the width of the twinned section is constant along its  
30  
31 length. The twin boundary is found to be an orthotwin<sup>63, 64</sup> (see Supporting Figure S5) and more  
32  
33 details about its position and propagation are given in Supporting Figure S6. Two additional  
34  
35  $\{10\}$  planes (usually  $\{103\}$ ) complete the faceting of the whole morphology. In contrast to the  
36  
37 complex higher index facets present where the lateral twin terminates on the top left hand side of  
38  
39 the droplet, the  $\{111\}$  and  $\{110\}$  facets are all atomically flat. A root mean square roughness of  
40  
41  $3.5\text{\AA}$  has been extracted using atomic force microscopy (AFM).  
42  
43  
44  
45  
46  
47  
48  
49

50  
51 In terms of the formation mechanism, a few observations should be made prior to describing a  
52  
53 growth scenario. First the nanosails retain two small  $\{110\}$  facets (extending directly from the  
54  
55 InAs “mast”) and two very large  $\{110\}$  facets of the original six  $\{110\}$  planes completing the  
56  
57  
58  
59  
60

1  
2  
3 perfectly hexagonal shape of an InSb nanowire. Secondly, all nanosails possess the same pure  
4 zinc blende crystal structure topped by a AuIn<sub>2</sub> alloy particle showing post-growth perfect strain-  
5 free epitaxial relationship with the semiconductor, exactly as InSb nanowires do<sup>61</sup>. Finally the  
6 growth conditions leading to the nanosail formation are obviously very close to those favorable  
7 for the growth of InSb nanowires since they both grow simultaneously, sometimes within sub-  
8 micron distances from each other, independently of the growth technique (MOVPE or MBE).  
9 Therefore, the nanosail formation clearly shares very strong links to the metal-assisted nanowire  
10 vapor liquid solid growth mechanism. In the same way, it was shown by several authors that  
11 under certain conditions, III-V nanowires can kink to other crystallographic directions<sup>65, 66</sup>,  
12 including to other polarities<sup>67</sup> or contain internal twins non-perpendicular to their elongation  
13 axis<sup>68, 69</sup>. In all the above examples it was either demonstrated or at least inferred that the alloyed  
14 seed particle was allowed to unpin from its standard {111} growth plane to wet more than one  
15 planes (multiple surfaces)<sup>70</sup>, including the nanowire sidewalls. Even during standard growth of  
16 diamond cubic or zinc blende nanowire crystals a corner oscillation has been confirmed by *in-*  
17 *situ* growth inside TEMs<sup>71-73</sup>.

18  
19  
20 Keeping in mind these considerations, Figure 2(f) illustrates our suggested phenomenological  
21 growth scenario to account for the formation of the InSb nanosails. When switching from As to  
22 Sb the droplet composition, phases and surface energy balance are changed dramatically. An  
23 increase in diameter occurs immediately after the introduction of Sb in the alloyed In(As,Sb)  
24 region a few nanometers above the InAs stem<sup>61</sup>. In agreement with a large set of published  
25 experimental results<sup>39, 70</sup>, the seed droplet is therefore allowed to unpin slightly from its position  
26 lying on the (-111) InSb plane to wet the sidewalls. Such a configuration has been shown to  
27 allow for new nucleation sites, and if two nuclei originating from two adjacent corners merge  
28  
29  
30  
31  
32  
33  
34  
35  
36  
37  
38  
39  
40  
41  
42  
43  
44  
45  
46  
47  
48  
49  
50  
51  
52  
53  
54  
55  
56  
57  
58  
59  
60

1  
2  
3 together, a grain boundary/twin can easily form. Illustrations of the morphological and structural  
4 signatures of this defect are shown in Supporting Figure S6. Once the inclined twin is formed the  
5 droplet wets multiple facets: the usual (-111) facet and a new {110} facet or ensemble of  
6 connected facets on its outer region (on the left, yellow pointed in Figure 2(f)). As the growth  
7 proceeds along the directions indicated in blue, the droplet will be stretched until the limit of its  
8 acceptable deformation in view of its surface tension. Such a dynamic modification of the  
9 surface area under the droplet has been described and modelled in detail in the case of twinning  
10 superlattices<sup>74, 75</sup>, where a further conceptual similarity lies in growth occurring on planes not  
11 perpendicular to the growth axis. After reaching its maximal surface tension the droplet will  
12 eventually unpin from the inclined lateral facet(s) pointed in yellow in Figure 2(f), resulting in  
13 the creation of the new facets that narrow the system. The situation shown in Figure 2(f) likely  
14 occurs at a very early stage of the nanosails formation, where its lateral extent does not differ  
15 much from that of a nanowire diameter. These sets of facets ({103} in the 3D model shown in  
16 Figure 2(e)) will depend on growth kinetics and adapt accordingly. As growth proceeds under  
17 the droplet, it may become more favorable for the droplet to stick to the {103}/(-111) triple  
18 phase boundary instead at the edge formed by the {110}/(-111) planes depicted on the right hand  
19 side in figure 2(f), leading to the creation of a new {-11-1} facet, exactly parallel to the bottom  
20 left one. An animated movie on the formation of the nanosails, based on atomic 3D models, can  
21 be found on-line<sup>76</sup>. Now that all of the key facets have been formed, the miniature nanosail  
22 grows *via* both vertical VLS and lateral Vapor Solid (VS) epitaxy to create the large surface area  
23 nanosheets observed. Future *in-situ* TEM growth studies could refine our understanding of the  
24 formation of such an original geometry<sup>77</sup>.  
25  
26  
27  
28  
29  
30  
31  
32  
33  
34  
35  
36  
37  
38  
39  
40  
41  
42  
43  
44  
45  
46  
47  
48  
49  
50  
51  
52  
53  
54  
55  
56  
57  
58  
59  
60

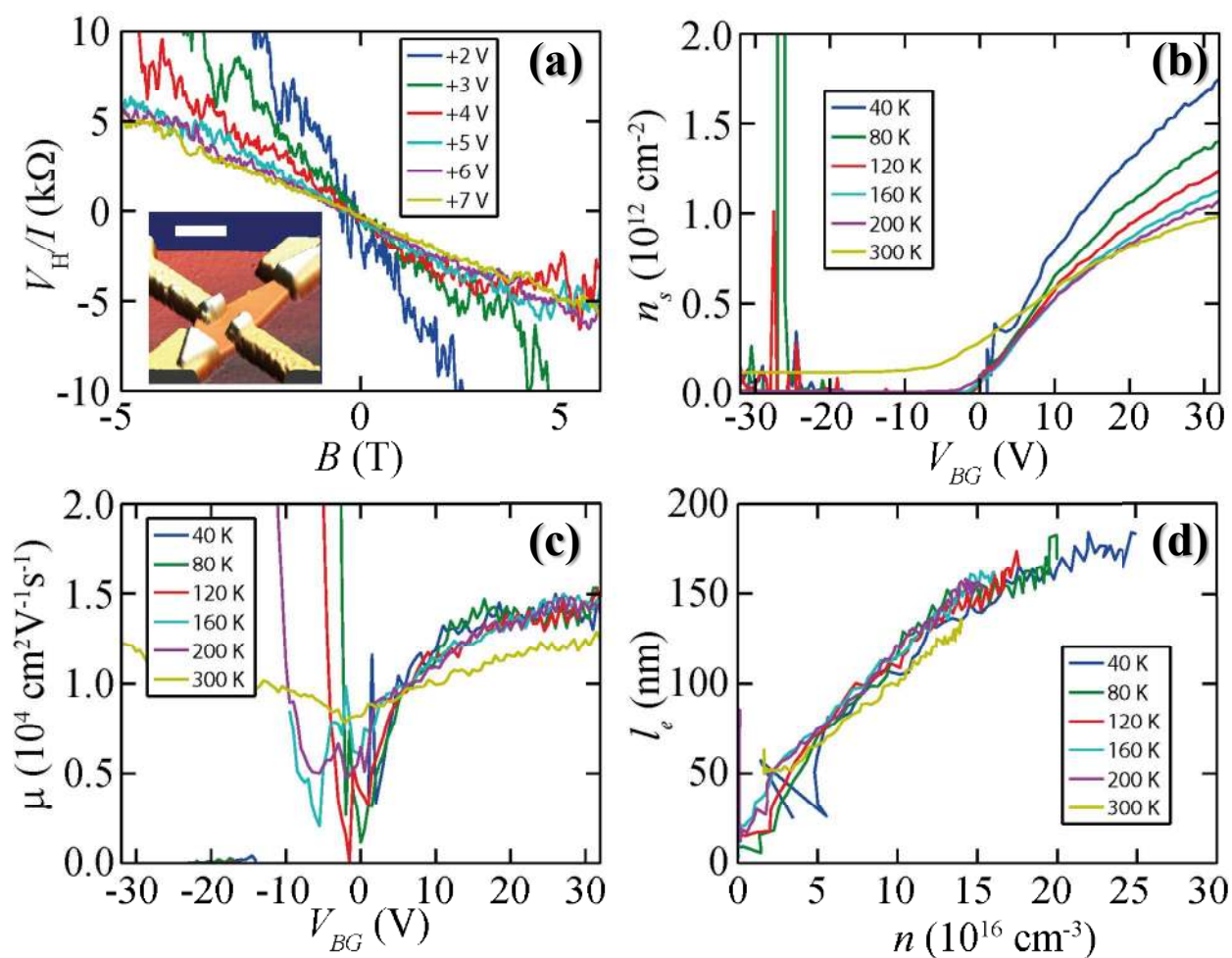


**Figure 3: Hall measurements on InSb nanosails.** (a) Hall voltage  $V_H$  as a function of the magnetic field applied perpendicular to the nanosail surface  $B$  for different voltages  $V_{BG}$  applied on the back-gate (values given in the legend) at a temperature of 2.1 K. Inset: AFM image of the four-terminal nanosail device (scale bar 500 nm). (b) Sheet electron density  $n_s$  as deduced from the Hall measurements using the single carrier model as a function of the back-gate voltage  $V_{BG}$

1  
2  
3 and for different temperatures (values given in the legend). (c) Electron mobility  $\mu$  as a function  
4 of the back-gate voltage  $V_{BG}$ . The mobility is calculated from the sheet resistance measured in  
5 the van der Pauw configuration and from the electron sheet density presented in panel (c). (d)  
6 Elastic mean free path  $l_e$  as a function of the bulk carrier density  $n$  assuming a homogeneous  
7 carrier distribution over the 70 nm thickness of the nanosail.  
8  
9

10  
11  
12  
13  
14  
15  
16 In order to assess the electronic quality of the InSb nanosails, we performed electrical  
17 measurements in the van der Pauw geometry, as shown inset of Figure 3(a), using a highly  
18 conductive  $n^+$  Si substrate covered by 225 nm thermal  $\text{SiO}_2$  oxide as a back gate to allow for  
19 tuning of the carrier density. This geometry allows direct access to the carrier density through the  
20 Hall effect, and to the intrinsic conductivity and carrier mobility through four-point  
21 measurements. Figure 3(a) shows the Hall voltage measured as a function of the magnetic field  
22 applied perpendicular to the nanosail surface. It follows the expected linear dependence with a  
23 negative sign corresponding to electrons. In the following the Hall voltage has been measured at  
24 +0.5 T and -0.5 T as a function of the gate voltage and temperature.  
25  
26  
27  
28  
29  
30  
31  
32  
33  
34  
35  
36  
37

38 At high temperature, the dependence of the Hall voltage on the back gate voltage is non  
39 monotonous, which is the signature of both electron and hole transport in a low band-gap  
40 material (see Supporting Information Figure S8). At lower temperature and positive gate voltage,  
41 only electrons participate in carrier transport, and we can therefore apply a single carrier model  
42 to determine the sheet electron density  $n_s$ , which is plotted as a function of the back gate voltage  
43 for different temperatures in Figure 3(b). At low temperature, the carrier density shows a  
44 threshold and linear variation for a limited range of gate voltages. A fit of the linear region (gate  
45 voltage range from +5 to +10 V) at 40 K gives a slope of  $(1.36 \pm 0.13) \times 10^{-4} \text{ C.cm}^{-2}$  and a  
46  
47  
48  
49  
50  
51  
52  
53  
54  
55  
56  
57  
58  
59  
60



1  
2  
3 threshold voltage of  $V_T = 0.3 \pm 0.5$  V. The slope is close to the expected value of  $1.5 \times 10^{-4}$  C.cm<sup>-2</sup>  
4  
5  
6 calculated from a plane capacitor model with the dielectric thickness of 225 nm.  
7

8  
9 We have measured the conductivity  $\sigma$  as a function of gate voltage and temperature using the  
10 van der Pauw method<sup>78</sup> (see Supporting Information Section SF). Similar to the Hall voltage, the  
11 conductivity at high temperature is a non-monotonous function of the gate voltage due to mixed  
12 electron and hole transport. At positive gate voltage, however the conductivity is dominated by  
13 electron transport due to the low mobility and density of holes. The electron mobility extracted in  
14 the single-carrier model is plotted as a function of the gate voltage for different temperatures in  
15 Figure 3(c). At room-temperature we find the mobility in our 70 nm-thick InSb nanosails to be  
16  $1.25 \times 10^4$  cm<sup>2</sup>V<sup>-1</sup>.s<sup>-1</sup>, a value less than that of bulk InSb ( $7.7 \times 10^4$  cm<sup>2</sup>V<sup>-1</sup>.s<sup>-1</sup>), but four times  
17 larger than 70 nm-thick InSb layers grown on GaAs, and equal to that of 300 nm thick InSb  
18 layers<sup>79, 80</sup>. This improvement relative to the best values for an InSb layer of similar thickness  
19 may be attributed to the absence of strain and dislocations that are inherent to the growth on  
20 substrate with large lattice mismatch, and demonstrates the significant potential of the nanosail  
21 geometry in realizing planar devices.  
22  
23  
24  
25  
26  
27  
28  
29  
30  
31  
32  
33  
34  
35  
36  
37  
38  
39

40 The mobility is weakly dependent on temperature (see Supporting Information SF.3), and is  
41 therefore most probably limited by defect scattering. Due to the absence of structural defects in  
42 the nanosail (apart from the single twin as discussed above), we attribute the origin of the  
43 scattering to defects close to the InSb surface, either traps in the SiO<sub>2</sub> dielectrics, at the  
44 SiO<sub>2</sub>/InSb interface or the top surface<sup>22</sup>. We have also deduced the electron mean free path  $l_e =$   
45  $v_F \tau_e$  from the average scattering time  $\tau_e = m^* \mu / e$ , and the 3D Fermi velocity  $v_F = \hbar k_F / m^* =$   
46  $(\hbar / m^*) (3\pi^2 n)^{1/3}$ , where  $n$  is the electron density.  $l_e$  is plotted as a function of  $n$  for different  
47 temperatures in Figure 3(d). That the mobility shows a weak temperature dependence suggests a  
48  
49  
50  
51  
52  
53  
54  
55  
56  
57  
58  
59  
60

1  
2  
3 scattering mechanism other than phonon scattering dominates. Previous work has shown  
4  
5 passivation to improve the mobility and mean-free path of nanostructures<sup>81-83</sup>. The relatively  
6  
7 large values of  $l_e$  found here holds realistic promise for the realization of ballistic transport in  
8  
9 future nanosail devices.  
10  
11

12  
13 In order to test the possibility of realizing ballistic quantum devices from our InSb nanosails,  
14  
15 we have fabricated a constriction on a nanosail by depositing two top gates as shown in the inset  
16  
17 of Figure 4(a). Such a constriction, also known as quantum point contact<sup>55,56</sup>, is expected to lead  
18  
19 to quasi-1D electronic transport. We emphasize here that such quasi-1D transport was expected  
20  
21 in InSb nanowires, but was only demonstrated at high magnetic field because back-scattering at  
22  
23 the contacts leads to a destruction of the signatures of 1D transport<sup>57</sup>. Up until now 1D transport  
24  
25 in InSb was only demonstrated in 2D electron gases formed in InSb heterostructures<sup>84</sup>, or in InSb  
26  
27 nanowires in the presence of an in-plane magnetic field<sup>57</sup>.  
28  
29  
30  
31  
32

33 The device with top gates showed a strong increase in resistance compared to devices without  
34  
35 top gates at zero applied top-gate voltage, which is presumably due to a depletion of the nanosail  
36  
37 below the top gates. We further observed that the resistance did not significantly vary with  
38  
39 application of top-gate voltage, giving further indication of this total depletion.  
40  
41  
42  
43

44 The conductance of a quasi-1D constriction is expected to be tuned either by changing the  
45  
46 width  $W$  of the constriction, or by changing the electron wave vector by changing the electron  
47  
48 density. In the following we have chosen to tune the carrier density in the constriction by using  
49  
50 the back gate instead of tuning the width of the constriction by using the top gate voltage due to  
51  
52 instabilities appearing when tuning the top gate, probably due to traps in the dielectric layer.  
53  
54  
55  
56  
57  
58  
59  
60

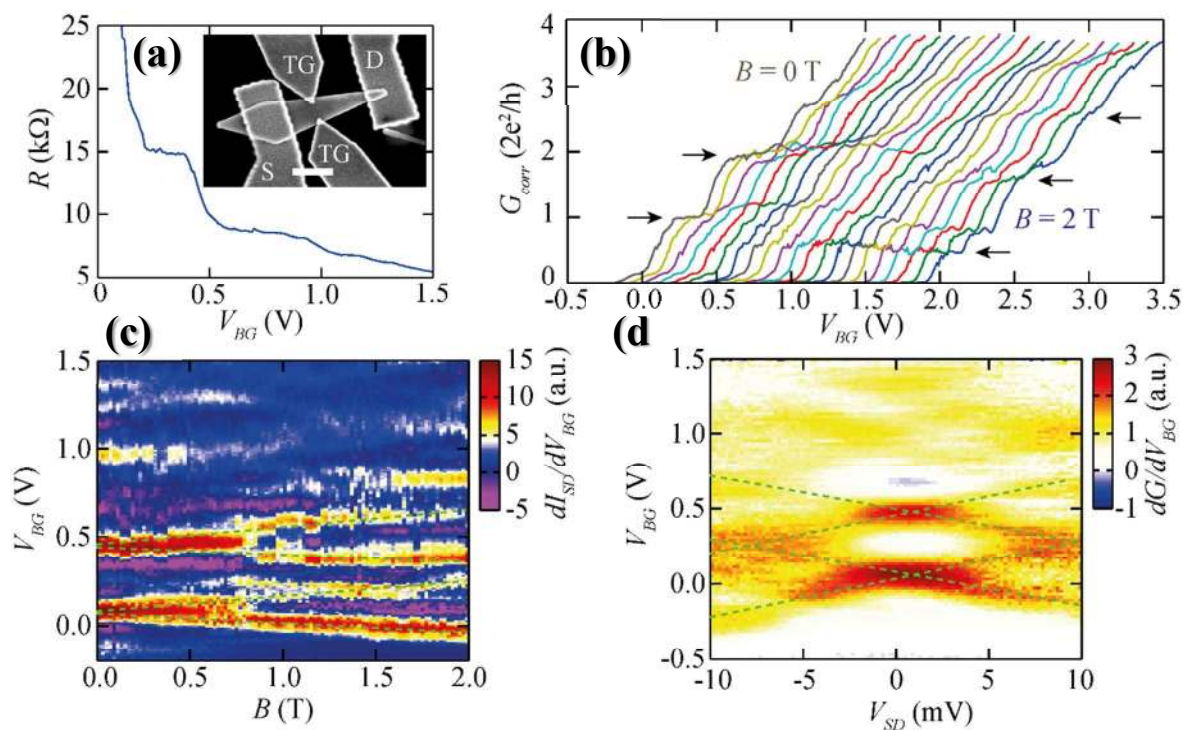


**Figure 4. Top-gated quantum point contact to an InSb nanosail.** (a) Two-point source-drain resistance of the device as a function of the back-gate voltage  $V_{BG}$  for a fixed voltage applied to the top-gates  $V_{TG} = +0.68$  V and measured at  $T = 6$  K. Inset: image of the top-gated quantum point contact device showing source and drain contacts, and two top gates electrically isolated from the nanosail by 10 nm of  $\text{HfO}_2$  deposited by atomic layer deposition. (b) Corrected conductance of the device obtained after removing a 2 k $\Omega$  series resistance from the two-terminal resistance, corresponding to the contact resistance (see main text), as a function of the back-gate voltage and varying the parallel magnetic field in steps of 0.1 T from 0 to 2 T. The measurement has been performed at  $T = 6$  K, and the curves have been laterally shifted by 0.1 V for clarity. The arrows emphasize the steps corresponding to conductance quantization. (c) Color map of  $G = dI_{SD}/dV_{BG}$  as a function of the parallel magnetic field and the back-gate voltage emphasizing the conductance steps. The green dashed lines show the splitting of the two first conductance steps measured at  $T = 2.1$  K. (d) Color-map of  $dG/dV_{BG}$  as a function of the source-

1  
2  
3 drain bias voltage  $V_{SD}$  and the back-gate voltage  $V_{BG}$  for  $V_{TG} = +0.68$  V and  $T = 6$  K. The green  
4  
5 dashed lines show the edge of the conduction steps.  
6  
7

8  
9 The two-terminal resistance of the top-gated device is shown as a function of the back-gate  
10 voltage for a fixed top-gate voltage  $V_{tg} = +0.68$  V in Figure 4(a). This curve, obtained at zero  
11 magnetic field, clearly shows two plateaux at about 15 k $\Omega$  (instead of  $h/2e^2 = 12.9$  k $\Omega$ ) and 8.5  
12 k $\Omega$  (instead of  $h/4e^2 = 6.5$  k $\Omega$ ) respectively. For quasi-1D electronic transport at zero magnetic  
13 field such plateaux are expected as  $h/2e^2 = 12.9$  k $\Omega$  and  $h/4e^2 = 6.5$  k $\Omega$ . We attribute the constant  
14 difference to a contact series resistance of about 2 k $\Omega$ , as well as the resistance of the nanosail  
15 outside the constriction. This resistance is compatible with the two-terminal resistance obtained  
16 in a device with no top gate (such as the one investigated in Figure 3). In order to emphasize  
17 further the quantification of the conductance in units of  $2e^2/h$ , as expected for a quantum point  
18 contact, we have plotted the two-terminal conductance corrected by the series resistance of 2 k $\Omega$   
19 in Figure 4(b). Here a magnetic field parallel to the plane of the nanosail is applied in order to  
20 split the 1D subbands. We see in this plot that the two plateaux at  $2e^2/h$  and  $4e^2/h$  disappear at a  
21 magnetic field of 2 T and give rise to plateaux at  $e^2/h$ ,  $3e^2/h$  and  $5e^2/h$ . Such behaviour can be  
22 explain by the splitting of the 1D sub-bands as a function of the magnetic field, and further  
23 confirms that the plateaux are related to 1D transport.  
24  
25  
26  
27  
28  
29  
30  
31  
32  
33  
34  
35  
36  
37  
38  
39  
40  
41  
42  
43  
44

45 We also investigated the splitting of the 1D sub-bands quantitatively as a function of applied  
46 magnetic field. In Figure 4(c) we plot the differential conductance  $G = dI_{SD}/dV_{BG}$  in order to  
47 emphasize the edges of the plateaux. In this plot we clearly observe the splitting of the two first  
48 sub-bands. This splitting should occur at a rate of  $g^* \mu_B B$ . In our case the splitting is 0.146 V/T for  
49 both sub-bands. In order to determine the lever arm of the back-gate (the change in Fermi energy  
50 as a function of the back-gate voltage), we have measured the non-linear conductance, i.e. the  
51  
52  
53  
54  
55  
56  
57  
58  
59  
60

1  
2  
3 change in the conductance as a function of the source-drain bias voltage. We see in Figure 4(d)  
4 that the edges of the plateaux split at finite source-drain bias voltage with a rate corresponding to  
5 a lever arm of 19.6 meV/V. We then determine a magnetic field splitting of 2.86 meV/T, and a  
6 Landé g-factor  $|g^*| = 49$ , which is close to the expected bulk value of 51.  
7  
8  
9

10  
11  
12  
13  
14 Finally, we investigated the effect of the top-gate voltage on the level spacing. From non-linear  
15 conductance measurements, we have determined the level spacing between the first two sub-  
16 bands at zero magnetic field (Supporting Information section SF.4). The energy for a top-gate  
17 voltage  $V_{TG} = +0.68$  V is  $E_2 - E_1 = 8.7$  meV, corresponding to a constriction of width 80 nm (for  
18 an infinite 1D square potential, with an electron effective mass  $m^* = m_0$ ). The level spacing for  
19  $V_{TG} = -1$  V is  $E_2 - E_1 = 11.1$  meV, corresponding to a constriction of width 70 nm. This  
20 dependence further confirms that the quasi-1D channel is formed in-between the two top-gates.  
21  
22  
23  
24  
25  
26  
27  
28  
29  
30

31 In conclusion we synthesized free-standing, high performance InSb nanostructures with a  
32 sheet-like morphology. This novel morphology is characterized by large atomically flat {110}  
33 surfaces and results from a single lateral twinning event. We measure a high electron mobility  
34 which is promising for both low power nanoelectronics and low temperature transport physics.  
35 Demonstration of quantized conductance in a quantum point contact at zero in-plane magnetic  
36 field further attests to material quality and the potential for spin-orbit quantum physics  
37 applications. We expect that the outlined growth mechanism may be generalized to other  
38 materials grown by VLS delivering a readily contacted 2D-like geometry for complex radial  
39 heterostructures and topological quantum physics experiments<sup>85</sup>. Future work on more advanced  
40 device geometries such as suspended nanomembrane devices<sup>86, 87</sup> or using dielectric/chemical  
41 passivation schemes<sup>81-83, 88</sup> could enhance their promising transport figures of merit even further.  
42  
43  
44  
45  
46  
47  
48  
49  
50  
51  
52  
53  
54  
55  
56  
57  
58  
59  
60

## ASSOCIATED CONTENT

**Supporting Information.** Methods, Growth, Characterization and Device Processing, SA. Statistics on the yield of different morphologies, SB (Figures S1-S3). Analysis of the InAs/InSb interface, SC (Figure S4). Presence of a unique twin boundary, SD (Figures S5, S6). Faceting of the nanosails, SE (Figure S7). Electrical measurements, SF (Figures S8-S11) This material is available free of charge via the Internet at <http://pubs.acs.org>.

## AUTHOR INFORMATION

**Corresponding Authors**

\*Emails: [philippe.caroff@anu.edu.au](mailto:philippe.caroff@anu.edu.au), [renaud.leturcq@list.lu](mailto:renaud.leturcq@list.lu), [arbiol@icrea.cat](mailto:arbiol@icrea.cat)

Present Address:

†SPEC, CEA, CNRS, Université Paris-Saclay, CEA Saclay 91191 Gif-sur-Yvette, France

**Author Contributions**

P.C. and R. L. conceived the idea for the research, co-lead the project and performed respectively the material growth/morphological analyses and most of the device processing/measurements.

M. M. performed the complete atomic resolution transmission electron microscopy analysis and built the 3D model as a result of the analysis, under the supervision of and with inputs from J.A., C. M., S.R.P., and P. C., whom altogether discussed and analyzed the growth and structural information. C. R. was involved in the device processing and measurements under the

1  
2  
3 supervision of R. L.. All authors commented on the work and provided valuable input throughout  
4  
5 the project. P. C. wrote the manuscript with significant contributions from all authors.  
6  
7

### 8 9 **Funding Sources**

10  
11 This research was supported in part by the French ANR through the TERADOT Project No.  
12  
13 ANR-11-JS04-002-01, the Ministry of Higher Education and Research, Nord-Pas de Calais and  
14  
15 Mid-Pyrénées Regional Council and FEDER through the “Contrat de Projets Etat Region  
16  
17 (CPER) 2007-2013”, IDEX WirOnSi, the Australian Research Council, through the Future  
18  
19 Fellowship program, grant number FT120100498, the Generalitat de Catalunya 2014 SGR 1638,  
20  
21 and the Spanish MINECO MAT2014-51480-ERC (e-ATOM).  
22  
23  
24

### 25 26 **Notes**

27  
28 The authors declare no competing financial interests.  
29  
30  
31  
32

### 33 34 **ACKNOWLEDGMENT**

35  
36 P.C., and R. L. thank Xavier Wallart for scientific discussions related to MBE growth,  
37  
38 Christophe Coinon and Jean-Louis Codron for technical support on the MBE, and Christophe  
39  
40 Boyaval for support on SEM imaging. P.C., S.R.P and J. A. thank Dr Jerry Tersoff for fruitful  
41  
42 discussions regarding the nanosail growth mechanisms. Tim burgess is acknowledged for  
43  
44 scientific discussions and for proof-reading the manuscript. The MBE growth has been  
45  
46 conducted in, and supported by, the EIPHY group lead by Xavier Wallart at IEMN. The  
47  
48 microscopy works have been conducted in the "Laboratorio de Microscopias Avanzadas" at  
49  
50 "Instituto de Nanociencia de Aragon - Universidad de Zaragoza". J.A. and M.d.l.M. thank the  
51  
52 LMA-INA for offering access to their instruments and expertise.  
53  
54  
55  
56  
57  
58  
59  
60

## REFERENCES

1. Yan, R.; Gargas, D.; Yang, P. *Nat. Photonics* **2009**, 3, (10), 569-576.
2. Vitiello, M. S.; Viti, L.; Coquillat, D.; Knap, W.; Ercolani, D.; Sorba, L. *APL Mater.* **2015**, 3, (2), 026104.
3. Riel, H.; Wernersson, L.-E.; Hong, M.; del Alamo, J. A. *MRS Bull.* **2014**, 39, (08), 668-677.
4. Wernersson, L.-E. *J. Appl. Phys.* **2015**, 117, (11), 112810.
5. Frolov, S. M.; Plissard, S. R.; Nadj-Perge, S.; Kouwenhoven, L. P.; Bakkers, E. P. A. M. *MRS Bull.* **2013**, 38, (10), 809-815.
6. Tomioka, K.; Fukui, T. *Nano Lett.* **2015**, 15, (11), 7189.
7. Svensson, J.; Dey, A. W.; Jacobsson, D.; Wernersson, L.-E. *Nano Lett.* **2015**.
8. Tomioka, K.; Yoshimura, M.; Fukui, T. *Nature* **2012**, 488, (7410), 189-192.
9. Lind, E.; Memisevic, E.; Dey, A. W.; Wernersson, L. E. *IEEE J. Electron Devices Soc.* **2015**, 3, (3), 96-102.
10. Yan, C.; Li, X.; Zhou, K.; Pan, A.; Werner, P.; Mensah, S. L.; Vogel, A. T.; Schmidt, V. *Nano Lett.* **2012**, 12, (4), 1799-1805.
11. Svensson, J.; Anttu, N.; Vainorius, N.; Borg, B. M.; Wernersson, L.-E. *Nano Lett.* **2013**, 13, (4), 1380-1385.
12. Duan, X.; Huang, Y.; Agarwal, R.; Lieber, C. M. *Nature* **2003**, 421, (6920), 241-245.
13. Qian, F.; Li, Y.; Gradecak, S.; Park, H.-G.; Dong, Y.; Ding, Y.; Wang, Z. L.; Lieber, C. M. *Nat. Mater.* **2008**, 7, (9), 701-706.
14. Chen, R.; Tran, T.-T. D.; Ng, K. W.; Ko, W. S.; Chuang, L. C.; Sedgwick, F. G.; Chang-Hasnain, C. *Nat. Photonics* **2011**, 5, (3), 170-175.



- 1  
2  
3  
4  
5  
6  
7  
8  
9  
10  
11  
12  
13  
14  
15  
16  
17  
18  
19  
20  
21  
22  
23  
24  
25  
26  
27  
28  
29  
30  
31  
32  
33  
34  
35  
36  
37  
38  
39  
40  
41  
42  
43  
44  
45  
46  
47  
48  
49  
50  
51  
52  
53  
54  
55  
56  
57  
58  
59  
60
15. Hicks, L. D.; Dresselhaus, M. S. *Phys. Rev. B* **1993**, 47, (24), 16631-16634.
  16. Boukai, A. I.; Bunimovich, Y.; Tahir-Kheli, J.; Yu, J.-K.; Goddard Iii, W. A.; Heath, J. R. *Nature* **2008**, 451, (7175), 168-171.
  17. Yamaguchi, S.; Matsumoto, T.; Yamazaki, J.; Kaiwa, N.; Yamamoto, A. *Appl. Phys. Lett.* **2005**, 87, (20), 201902.
  18. Mingo, N. *Appl. Phys. Lett.* **2004**, 84, (14), 2652-2654.
  19. Uryupin, O. N.; Vedernikov, M. V.; Shabal'din, A. A.; Ivanov, Y. V.; Kumzerov, Y. A.; Fokin, A. V. *J. Electron. Mater.* **2009**, 38, (7), 990-993.
  20. Mensch, P.; Karg, S.; Schmidt, V.; Gotsmann, B.; Schmid, H.; Riel, H. *Appl. Phys. Lett.* **2015**, 106, (9), 093101.
  21. Nilsson, H. A.; Caroff, P.; Thelander, C.; Larsson, M.; Wagner, J. B.; Wernersson, L.-E.; Samuelson, L.; Xu, H. Q. *Nano Lett.* **2009**, 9, (9), 3151-3156.
  22. Gül, Ö.; J. van Woerkom, D.; Weperen, I. v.; Car, D.; Plissard, S. R.; Bakkers, E., P. A. M.; Kouwenhoven, L., P. *Nanotechnol.* **2015**, 26, (21), 215202.
  23. Nilsson, H. A.; Karlström, O.; Larsson, M.; Caroff, P.; Pedersen, J. N.; Samuelson, L.; Wacker, A.; Wernersson, L. E.; Xu, H. Q. *Phys. Rev. Lett.* **2010**, 104, (18), 186804.
  24. Pribiag, V. S.; Nadj Perge, S.; Frolov, S. M.; van den Berg, J. W. G.; van Weperen, I.; Plissard, S. R.; Bakkers, E. P. A. M.; Kouwenhoven, L. P. *Nat. Nanotechnol.* **2013**, 8, (3), 170-174.
  25. Nadj-Perge, S.; Pribiag, V. S.; van den Berg, J. W. G.; Zuo, K.; Plissard, S. R.; Bakkers, E. P. A. M.; Frolov, S. M.; Kouwenhoven, L. P. *Phys. Rev. Lett.* **2012**, 108, (16), 166801.
  26. van den Berg, J. W. G.; Nadj-Perge, S.; Pribiag, V. S.; Plissard, S. R.; Bakkers, E. P. A. M.; Frolov, S. M.; Kouwenhoven, L. P. *Phys. Rev. Lett.* **2013**, 110, (6), 066806.

- 1  
2  
3 27. Mourik, V.; Zuo, K.; Frolov, S. M.; Plissard, S. R.; Bakkers, E. P. A. M.; Kouwenhoven,  
4 L. P. *Science* **2012**, 336, (6084), 1003-1007.  
5  
6  
7  
8 28. Deng, M. T.; Yu, C. L.; Huang, G. Y.; Larsson, M.; Caroff, P.; Xu, H. Q. *Nano Lett.*  
9  
10 **2012**, 12, (12), 6414-6419.  
11  
12 29. Deng, M. T.; Yu, C. L.; Huang, G. Y.; Larsson, M.; Caroff, P.; Xu, H. Q. *Sci. Rep.* **2014**,  
13 4, 7261.  
14  
15  
16  
17 30. Borg, B. M.; Wernersson, L.-E. *Nanotechnol.* **2013**, 24, (20), 202001.  
18  
19 31. Caroff, P.; Messing, M., E.; Borg, B. M.; Dick, K., A.; Deppert, K.; Wernersson, L.-E.  
20  
21 *Nanotechnol.* **2009**, 20, (49), 495606.  
22  
23 32. Li, A.; Sibirev, N. V.; Ercolani, D.; Dubrovskii, V. G.; Sorba, L. *Cryst. Growth Des.*  
24  
25 **2013**, 13, (2), 878-882.  
26  
27  
28 33. Plissard, S. R.; Slapak, D. R.; Verheijen, M. A.; Hocevar, M.; Immink, G. W. G.; van  
29  
30 Weperen, I.; Nadj-Perge, S.; Frolov, S. M.; Kouwenhoven, L. P.; Bakkers, E. P. A. M. *Nano*  
31  
32 *Lett.* **2012**, 12, (4), 1794-1798.  
33  
34  
35 34. Park, H. D.; Prokes, S. M.; Twigg, M. E.; Ding, Y.; Wang, Z. L. *J. Cryst. Growth*  
36  
37 **2007**, 304, (2), 399-401.  
38  
39  
40 41. Caroff, P.; Wagner, J. B.; Dick, K. A.; Nilsson, H. A.; Jeppsson, M.; Deppert, K.;  
42  
43 Samuelson, L.; Wallenberg, L. R.; Wernersson, L.-E. *Small* **2008**, 4, (7), 878-882.  
44  
45 46. Ercolani, D.; Rossi, F.; Li, A.; Roddaro, S.; Grillo, V.; Salviati, G.; Beltram, F.; Sorba, L.  
47  
48 *Nanotechnol.* **2009**, 20, (50), 505605.  
49  
50 51. Thelander, C.; Caroff, P.; Plissard, S.; Dick, K. A. *Appl. Phys. Lett.* **2012**, 100, (23),  
52  
53 232105.  
54  
55  
56  
57  
58  
59  
60

- 1  
2  
3  
4  
5  
6  
7  
8  
9  
10  
11  
12  
13  
14  
15  
16  
17  
18  
19  
20  
21  
22  
23  
24  
25  
26  
27  
28  
29  
30  
31  
32  
33  
34  
35  
36  
37  
38  
39  
40  
41  
42  
43  
44  
45  
46  
47  
48  
49  
50  
51  
52  
53  
54  
55  
56  
57  
58  
59  
60
38. Gorji Ghalamestani, S.; Ek, M.; Ganjipour, B.; Thelander, C.; Johansson, J.; Caroff, P.; Dick, K. A. *Nano Lett.* **2012**, 12, (9), 4914-4919.
39. Plissard, S. R.; van Weperen, I.; Car, D.; Verheijen, M. A.; Immink, G. W. G.; Kammhuber, J.; Cornelissen, L. J.; Szombati, D. B.; Geresdi, A.; Frolov, S. M.; Kouwenhoven, L. P.; Bakkers, E. P. A. M. *Nat. Nanotechnol.* **2013**, 8, (11), 859-864.
40. Car, D.; Wang, J.; Verheijen, M. A.; Bakkers, E. P. A. M.; Plissard, S. R. *Adv. Mater.* **2014**, 26, (28), 4875-4879.
41. Uccelli, E.; Arbiol, J.; Magen, C.; Krogstrup, P.; Russo-Averchi, E.; Heiss, M.; Mugny, G.; Morier-Genoud, F.; Nygård, J.; Morante, J. R.; Fontcuberta i Morral, A. *Nano Lett.* **2011**, 11, (9), 3827-3832.
42. Utama, M. I. B.; de la Mata, M.; Magen, C.; Arbiol, J.; Xiong, Q. *Adv. Funct. Mater.* **2013**, 23, (13), 1636-1646.
43. Dayeh, S. A.; Wang, J.; Li, N.; Huang, J. Y.; Gin, A. V.; Picraux, S. T. *Nano Lett.* **2011**, 11, (10), 4200-4206.
44. Blömers, C.; Grap, T.; Lepsa, M. I.; Moers, J.; Trelenkamp, S.; Grützmacher, D.; Lüth, H.; Schäpers, T. *Appl. Phys. Lett.* **2012**, 101, (15), 152106.
45. Storm, K.; Halvardsson, F.; Heurlin, M.; Lindgren, D.; Gustafsson, A.; Wu, P. M.; Monemar, B.; Samuelson, L. *Nat. Nanotechnol.* **2012**, 7, (11), 718-722.
46. Schelter, J.; Bohr, D.; Trauzettel, B. *Phys. Rev. B* **2010**, 81, (19), 195441.
47. Nikoobakht, B.; Li, X. *ACS Nano* **2012**, 6, (3), 1883-1887.
48. Arab, S.; Chi, C.-Y.; Shi, T.; Wang, Y.; Dapkus, D. P.; Jackson, H. E.; Smith, L. M.; Cronin, S. B. *ACS Nano* **2015**, 9, (2), 1336-1340.

- 1  
2  
3 49. Chang, C.-C.; Chi, C.-Y.; Chen, C.-C.; Huang, N.; Arab, S.; Qiu, J.; Povinelli, M.;  
4  
5 Dapkus, P. D.; Cronin, S. *Nano Res.* **2014**, 7, (2), 163-170.  
6  
7  
8 50. Aagesen, M.; Johnson, E.; Sorensen, C. B.; Mariager, S. O.; Feidenhans'l, R.; Spiecker,  
9  
10 E.; Nygard, J.; Lindelof, P. E. *Nat. Nanotechnol.* **2007**, 2, (12), 761-764.  
11  
12  
13 51. Conesa-Boj, S.; Russo-Averchi, E.; Dalmau-Mallorqui, A.; Trevino, J.; Pecora, E. F.;  
14  
15 Forestiere, C.; Handin, A.; Ek, M.; Zweifel, L.; Wallenberg, L. R.; Ruffer, D.; Heiss, M.;  
16  
17 Troadec, D.; Dal Negro, L.; Caroff, P.; Fontcuberta i Morral, A. *ACS Nano* **2012**, 6, (12), 10982-  
18  
19 10991.  
20  
21  
22 52. Hsu, C.-W.; Chen, Y.-F.; Su, Y.-K. *Nanoscale Res. Lett.* **2012**, 7, (1), 642.  
23  
24  
25 53. Chi, C.-Y.; Chang, C.-C.; Hu, S.; Yeh, T.-W.; Cronin, S. B.; Dapkus, P. D. *Nano Lett.*  
26  
27 **2013**, 13, (6), 2506-2515.  
28  
29  
30 54. Tutuncuoglu, G.; de la Mata, M.; Deiana, D.; Potts, H.; Matteini, F.; Arbiol, J.;  
31  
32 Fontcuberta i Morral, A. *Nanoscale* **2015**, 7, (46), 19453-19460.  
33  
34  
35 55. Wharam, D. A.; Thornton, T. J.; Newbury, R.; Pepper, M.; Ahmed, H.; Frost, J. E. F.;  
36  
37 Hasko, D. G.; Peacock, D. C.; Ritchie, D. A.; Jones, G. A. C. *J. Phys. C: Solid State Phys.* **1988**,  
38  
39 21, (8), L209.  
40  
41  
42 56. van Wees, B. J.; van Houten, H.; Beenakker, C. W. J.; Williamson, J. G.; Kouwenhoven,  
43  
44 L. P.; van der Marel, D.; Foxon, C. T. *Phys. Rev. Lett.* **1988**, 60, (9), 848-850.  
45  
46  
47 57. van Weperen, I.; Plissard, S. R.; Bakkers, E. P. A. M.; Frolov, S. M.; Kouwenhoven, L.  
48  
49 *P. Nano Lett.* **2013**, 13, (2), 387-391.  
50  
51  
52 58. Bernal, S.; Botana, F. J.; Calvino, J. J.; López-Cartes, C.; Pérez-Omil, J. A.; Rodríguez-  
53  
54 Izquierdo, J. M. *Ultramicroscopy* **1998**, 72, (3-4), 135-164.  
55  
56  
57  
58  
59  
60

- 1  
2  
3  
4  
5  
6  
7  
8  
9  
10  
11  
12  
13  
14  
15  
16  
17  
18  
19  
20  
21  
22  
23  
24  
25  
26  
27  
28  
29  
30  
31  
32  
33  
34  
35  
36  
37  
38  
39  
40  
41  
42  
43  
44  
45  
46  
47  
48  
49  
50  
51  
52  
53  
54  
55  
56  
57  
58  
59  
60
59. Arbiol, J.; Cirera, A.; Peiró, F.; Cornet, A.; Morante, J. R.; Delgado, J. J.; Calvino, J. J. *Appl. Phys. Lett.* **2002**, 80, (2), 329-331.
60. de la Mata, M.; Magen, C.; Gazquez, J.; Utama, M. I. B.; Heiss, M.; Lopatin, S.; Furtmayr, F.; Fernández-Rojas, C. J.; Peng, B.; Morante, J. R.; Rurali, R.; Eickhoff, M.; Fontcuberta i Morral, A.; Xiong, Q.; Arbiol, J. *Nano Lett.* **2012**, 12, (5), 2579-2586.
61. de la Mata, M.; Magén, C.; Caroff, P.; Arbiol, J. *Nano Lett.* **2014**, 14, (11), 6614-6620.
62. Philipose, U.; Gopal, S.; Salfi, J.; Harry, E. R. *Semicond. Sci. Technol.* **2010**, 25, (7), 075004.
63. Cohen, D.; McKernan, S.; Carter, C. B. *Microsc. Microanal.* **1999**, 5, (03), 173-186.
64. Holt, D. B. *J Mater Sci* **1984**, 19, (2), 439-446.
65. Wang, J.; Plissard, S. R.; Verheijen, M. A.; Feiner, L.-F.; Cavalli, A.; Bakkers, E. P. A. *M. Nano Lett.* **2013**, 13, (8), 3802-3806.
66. Fonseka, H. A.; Caroff, P.; Wong-Leung, J.; Ameruddin, A. S.; Tan, H. H.; Jagadish, C. *ACS Nano* **2014**, 8, (7), 6945-6954.
67. Yuan, X.; Caroff, P.; Wong-Leung, J.; Fu, L.; Tan, H. H.; Jagadish, C. *Adv. Mater.* **2015**, 27, (40), 6096-6103.
68. Oliveira, D. S.; Tizei, L. H. G.; Li, A.; Vasconcelos, T. L.; Senna, C. A.; Archanjo, B. S.; Ugarte, D.; Cotta, M. A. *Nanoscale* **2015**, 7, (29), 12722-12727.
69. Yuan, X.; Caroff, P.; Wong-Leung, J.; Tan, H. H.; Jagadish, C. *Nanoscale* **2015**, 7, (11), 4995-5003.
70. Hocevar, M.; Immink, G.; Verheijen, M.; Akopian, N.; Zwiller, V.; Kouwenhoven, L.; Bakkers, E. *Nat. Commun.* **2012**, 3, 1266.

- 1  
2  
3  
4  
5  
6  
7  
8  
9  
10  
11  
12  
13  
14  
15  
16  
17  
18  
19  
20  
21  
22  
23  
24  
25  
26  
27  
28  
29  
30  
31  
32  
33  
34  
35  
36  
37  
38  
39  
40  
41  
42  
43  
44  
45  
46  
47  
48  
49  
50  
51  
52  
53  
54  
55  
56  
57  
58  
59  
60
71. Oh, S. H.; Chisholm, M. F.; Kauffmann, Y.; Kaplan, W. D.; Luo, W.; Rühle, M.; Scheu, C. *Science* **2010**, 330, (6003), 489-493.
72. Gamalski, A. D.; Ducati, C.; Hofmann, S. *J. Phys. Chem. C* **2011**, 115, (11), 4413-4417.
73. Wen, C. Y.; Tersoff, J.; Hillerich, K.; Reuter, M. C.; Park, J. H.; Kodambaka, S.; Stach, E. A.; Ross, F. M. *Phys. Rev. Lett.* **2011**, 107, (2), 025503.
74. Algra, R. E.; Verheijen, M. A.; Borgstrom, M. T.; Feiner, L.-F.; Immink, G.; van Enckevort, W. J. P.; Vlieg, E.; Bakkers, E. P. A. M. *Nature* **2008**, 456, (7220), 369-372.
75. Burgess, T.; Breuer, S.; Caroff, P.; Wong-Leung, J.; Gao, Q.; Hoe Tan, H.; Jagadish, C. *ACS Nano* **2013**, 7, (9), 8105-8114.
76. <http://www.gaen.cat/research/279>.
77. Gamalski, A. D.; Voorhees, P. W.; Ducati, C.; Sharma, R.; Hofmann, S. *Nano Lett.* **2014**, 14, (3), 1288-1292.
78. Pauw, L. J. v. d. *Philips Tech. Rev.* **1958**, 13, 220.
79. Zhang, T.; Clowes, S. K.; Debnath, M.; Bennett, A.; Roberts, C.; Harris, J. J.; Stradling, R. A.; Cohen, L. F.; Lyford, T.; Fewster, P. F. *Appl. Phys. Lett.* **2004**, 84, (22), 4463-4465.
80. Zhang, T.; Harris, J. J.; Branford, W. R.; Bugoslavsky, Y. V.; Clowes, S. K.; Cohen, L. F.; Husmann, A.; Solin, S. A. *Appl. Phys. Lett.* **2006**, 88, (1), 012110.
81. Ko, H.; Takei, K.; Kapadia, R.; Chuang, S.; Fang, H.; Leu, P. W.; Ganapathi, K.; Plis, E.; Kim, H. S.; Chen, S.-Y.; Madsen, M.; Ford, A. C.; Chueh, Y.-L.; Krishna, S.; Salahuddin, S.; Javey, A. *Nature* **2010**, 468, (7321), 286-289.
82. Ford, A. C.; Kumar, S. B.; Kapadia, R.; Guo, J.; Javey, A. *Nano Lett.* **2012**, 12, (3), 1340-1343.

- 1  
2  
3  
4  
5  
6  
7  
8  
9  
10  
11  
12  
13  
14  
15  
16  
17  
18  
19  
20  
21  
22  
23  
24  
25  
26  
27  
28  
29  
30  
31  
32  
33  
34  
35  
36  
37  
38  
39  
40  
41  
42  
43  
44  
45  
46  
47  
48  
49  
50  
51  
52  
53  
54  
55  
56  
57  
58  
59  
60
83. Potts, H.; Friedl, M.; Amaduzzi, F.; Tang, K.; Tütüncüoğlu, G.; Matteini, F.; Alarcon Lladó, E.; McIntyre, P. C.; Fontcuberta i Morral, A. *Nano Lett.* **2015**.
84. Goel, N.; Graham, J.; Keay, J. C.; Suzuki, K.; Miyashita, S.; Santos, M. B.; Hirayama, Y. *Physica E* **2005**, 26, (1-4), 455-459.
85. Gluschke, J. G.; Leijnse, M.; Ganjipour, B.; Dick, K. A.; Linke, H.; Thelander, C. *ACS Nano* **2015**, 9, (7), 7033-7040.
86. Bolotin, K. I.; Sikes, K. J.; Jiang, Z.; Klima, M.; Fudenberg, G.; Hone, J.; Kim, P.; Stormer, H. L. *Solid State Commun.* **2008**, 146, (9–10), 351-355.
87. Schmidt, M.; Schneider, G.; Heyn, C.; Stemmann, A.; Hansen, W. J. *Electron. Mater.* **2012**, 41, (6), 1286-1289.
88. Suyatin, D. B.; Thelander, C.; Björk, M. T.; Maximov, I.; Samuelson, L. *Nanotechnology* **2007**, 18, (10), 105307.

FOR TOC ONLY

